Iranian Journal of Astronomy and Astrophysics
Vol. 12, No. 3, Summer 2025, 267–290
©Available online at http://ijaa.du.ac.ir
DOI: 10.22128/ijaa.2026.3207.1241
Online ISSN: 2383–403X

Iranian Journal of Astronomy and Astrophysics

Review Paper

A Review of Solar Spectral Analysis

Somaye Hosseini Rad*[1] · Hasan Rezaei[2] · Mehdi Simiari[3] · Hossein Safari[4]

[1] Department of Physics, Faculty of Science, University of Zanjan, University Blvd., P.O. Box 45371-38791, Zanjan, Iran;
*E-mail: hosseinirad@alumni.znu.ac.ir

[2] Department of Geography, Faculty of Basic Sciences, Imam Ali Nazaja University, P.O. Box 1317893471, Tehran, Iran;
E-mail: rezaei_hasan63@yahoo.com

[3] Department of physics, Faculty of Science, Imam Ali University, P.O. Box 1317893471, Tehran, Iran;
E-mail: mehdi.simiari@gmail.com

[4] Department of Physics, Faculty of Science, University of Zanjan, University Blvd., P.O. Box 45371-38791, Zanjan, Iran;
E-mail: safari@znu.ac.ir

Received: 28 December 2025; **Accepted:** 9 January 2026; **Published:** 18 January 2026

Abstract. Solar spectral lines are among the most powerful diagnostics of plasma conditions in the solar atmosphere, providing constraints on temperature, density, flows, turbulence, magnetic fields, and energy release processes. High-resolution ultraviolet and X-ray observations reveal that solar line profiles often deviate from idealized symmetric Gaussian shapes, exhibiting excess broadening, asymmetries, and multi-component structures from the chromosphere to the flaring corona. This review presents an overview of the physical mechanisms governing solar spectral line formation, symmetry, asymmetry, and broadening, with emphasis on ultraviolet and extreme-ultraviolet diagnostics. We discuss the roles of thermal and non-thermal Doppler motions, unresolved flows, wave activity, magnetic and Stark effects, opacity-related processes, and instrumental broadening. Particular attention is given to transition-region lines, where multiple plasma components and highly dynamic heating processes produce complex, non-Gaussian profiles. We also review widely used methods for spectral line analysis, including single- and multi-Gaussian fitting, Lorentzian and Voigt representations, and Bayesian Markov Chain Monte Carlo approaches that enable robust parameter estimation and model comparison. Recent IRIS observations show that asymmetric Si IV line profiles are widespread in flaring and non-flaring conditions and often require multi-component modeling. Finally, we outline current challenges and emerging directions in solar spectroscopy, including instrumental calibration, cross-instrument consistency, and physics-informed analysis techniques. Future coordinated observations and improved inversion methods are expected to enhance the diagnostic potential of solar spectral lines and advance our understanding of plasma heating, magnetic reconnection, and energy transport in the solar atmosphere.

Keywords: Solar Spectroscopy, Spectral Line Broadening, Line Profile Asymmetry, Doppler Diagnostics, Transition Region, Coronal Plasma.

* *Corresponding author*

1 Introduction

Solar radiation spans an extraordinarily broad range of the electromagnetic spectrum, extending continuously from long-wavelength radio emission to hard X-rays and gamma rays. Each spectral window carries unique diagnostic information about physical processes operating in distinct layers of the solar atmosphere, from the convective photosphere through the highly structured chromosphere and transition region, up to the magnetically dominated corona and the nascent solar wind. Because radiative emission responds sensitively to plasma temperature, ionization state, density, velocity fields, magnetic topology, and non-thermal particle populations, solar spectroscopy has long served as a cornerstone of heliophysics and plasma astrophysics [1–3]. Through detailed analysis of spectral line intensities, shapes, widths, and asymmetries, it is possible to probe multi-scale energy transport, magnetic reconnection, wave dissipation, turbulence, and impulsive heating processes that are otherwise inaccessible to direct measurement.

High-resolution spectroscopic observations have enabled quantitative characterization of line-formation processes across all atmospheric layers. Photospheric absorption lines provide precise diagnostics of convection, granulation, oscillations, and elemental abundances [4]. In the chromosphere, strong resonance lines such as Ca II H&K, Mg II h&k, and Hα reveal shock propagation, fibril dynamics, and the interaction between plasma flows and expanding magnetic canopies [5,6]. The transition region (TR), characterized by steep temperature gradients and rapid temporal variability, is best probed by ultraviolet lines of ions such as C II, Si IV, and O VI, which respond sensitively to impulsive heating, reconnection outflows, and mass exchange between the chromosphere and corona [7,8]. At coronal temperatures, EUV and X-ray emission lines encode information on heating rates, magnetic confinement, wave activity, nanoflare-driven dynamics, and departures from Maxwellian particle distributions [9,10].

A wide range of observable spectral properties—line centroid shifts, thermal and non-thermal widths, enhanced wings, asymmetries, opacity ratios, and multi-component structures—carry signatures of the underlying plasma physics. These observables reflect the combined effects of unresolved bulk flows, turbulence, Alfvénic waves, magnetic reconnection, radiative-transfer processes, and instrumental response [11–13]. In particular, deviations from symmetric Gaussian profiles have emerged as a key diagnostic of fine-scale dynamics and multi-thermal structuring along the line of sight, especially in the highly dynamic transition region and flaring corona.

Major advances in solar spectroscopy have been driven by space-based instrumentation, which overcomes atmospheric absorption and enables continuous access to ultraviolet and X-ray wavelengths. Early milestones were achieved with Yohkoh/BCS and SOHO/SUMER, which provided the first systematic X-ray and UV spectral diagnostics of coronal heating and transition-region dynamics [14,15]. Subsequent missions, including Hinode/EIS [16], IRIS [17], SDO/EVE, and more recently Solar Orbiter instruments such as STIX and SPICE [18,19], have delivered unprecedented spectral, spatial, and temporal resolution. These observations have enabled routine detection of Doppler shifts at the level of a few $\mathrm{km\,s^{-1}}$, characterization of non-thermal line broadening, and identification of subtle asymmetries associated with reconnection jets, chromospheric evaporation, and turbulent flows.

The growing volume and complexity of spectroscopic data have motivated the development of advanced analysis techniques that go beyond classical least-squares fitting. Modern solar spectroscopy increasingly relies on Bayesian inference, forward modeling, and statistical model comparison to robustly extract physical parameters and quantify uncertainties [20,21]. Multi-component Gaussian, Lorentzian, and Voigt representations are now routinely employed to describe asymmetric and non-Gaussian line profiles, while physically motivated

constraints are used to mitigate parameter degeneracy. These approaches have proven particularly powerful in the interpretation of transition-region lines observed by IRIS, where multiple plasma components frequently coexist within a single resolution element.

In recent years, machine-learning (ML) techniques have become increasingly important for analyzing solar spectral data. Convolutional neural networks (CNNs) have been applied successfully to accelerate the inversion of spectropolarimetric Stokes profiles, allowing rapid retrieval of atmospheric parameters that previously required computationally intensive forward modeling [22]. Likewise, supervised and deep-learning methods have been used to extract thermodynamic information from high-resolution IRIS spectra, demonstrating ML's capability to recover temperature, density, and velocity structures from large observational datasets [23]. At the same time, compressed-sensing and multi-component decomposition approaches offer an efficient way to separate overlapping spectral features, detect asymmetric or multi-flow structures, and classify complex line profiles in UV and X-ray spectra [24]. Together, these physically informed ML techniques, when combined with traditional spectral diagnostics, provide a scalable framework to fully exploit the increasing volume and complexity of solar spectroscopic observations expected from next-generation instruments.

This review brings together classical foundations and recent developments in solar spectral physics, with a particular focus on line broadening mechanisms, symmetry and asymmetry diagnostics, and modern methods for spectral line profile analysis. By synthesizing observational results, theoretical interpretations, numerical modeling, and data-driven techniques, we aim to provide a coherent framework for understanding how solar spectral lines encode the multi-scale dynamics and energetics of the solar atmosphere, and to outline emerging directions for future spectroscopic studies.

2 Background on Solar Spectral Physics

Solar spectral physics forms the basis for interpreting radiation emitted from the various layers of the solar atmosphere. Spectral lines observed in the UV, EUV, and X-ray ranges sample plasma spanning more than six orders of magnitude in temperature, from the cool chromosphere ($\sim 10^4$ K) to the hot, flaring corona ($\sim 10^7$ K). Extracting physical information from these lines relies on a synthesis of atomic physics, radiative-transfer theory, and magnetohydrodynamic (MHD) plasma concepts [1,2,9].

Line formation in the solar atmosphere is governed primarily by collisional excitation, radiative decay, resonant scattering, and departures from local thermodynamic equilibrium. In the tenuous corona, optically thin conditions usually apply, allowing observed intensities to be related directly to emission measures and atomic parameters [13,25]. In contrast, chromospheric diagnostics such as Mg II h&k and Hα are strongly affected by radiative-transfer and partial frequency redistribution effects, necessitating detailed non-LTE modeling [26,27].

Magnetic fields play a central role in structuring the solar atmosphere and shaping spectral signatures. Polarization and line-profile modifications arising from the Zeeman and Hanle effects provide key diagnostics of magnetic fields [28]. In the corona, magnetic confinement and heating produce multi-thermal plasma conditions that manifest as Doppler shifts, non-thermal line broadening, and complex profile shapes [16,29].

Dynamic processes such as waves, turbulence, reconnection-driven flows, and evaporation–condensation cycles leave clear imprints on spectral lines. High-resolution observations reveal ubiquitous small-scale activity, including transition-region explosive events, nanoflare-related upflows, and coronal rain [17,30,31]. These signatures underpin spectroscopic diagnostics of mass transport, energy release, and heating throughout the solar atmosphere.

Contemporary spectral analysis depends critically on atomic databases such as CHI-

ANTI [25,32], which provide the atomic data needed to interpret observations quantitatively. Combined with numerical MHD and radiative-transfer simulations (e.g., Bifrost and RADYN), these databases enable forward modeling of spectral line formation under realistic solar conditions [33,34]. Together, such tools form the foundation of modern solar spectral physics.

3 Observational Techniques and Instruments

Over the past several decades, advances in space-based solar spectroscopy have fundamentally transformed our understanding of plasma processes throughout the solar atmosphere. Owing to the extreme thermal stratification of the Sun—ranging from photospheric temperatures of ∼6000 K to flaring coronal plasma exceeding $\sim 10^7$ K—its spectral emission spans a broad wavelength range, necessitating the use of multiple, complementary instruments for comprehensive diagnostics [1,2]. High-resolution UV and X-ray spectrometers have enabled precise measurements of Doppler shifts, non-thermal line broadening, opacity effects, and spectral asymmetries associated with dynamic phenomena such as magnetic reconnection, chromospheric evaporation, and transition-region explosive events [3,7,35].

The evolution of instrumental design—from early Bragg Crystal Spectrometers onboard *Yohkoh* [14] to the EUV Imaging Spectrometer (EIS) aboard *Hinode* [16], the high-resolution IRIS spectrograph [17], and more recently the spectrometers on *Solar Orbiter*, including SPICE and STIX [18,36]—has progressively expanded the accessible spectral domain. These instruments achieve sub-arcsecond spatial resolution, spectral resolving powers exceeding $R \sim 10^4$, and temporal cadences suitable for capturing rapidly evolving flare kernels, transition-region bursts, and turbulent coronal flows [37,38].

Beyond slit-based spectrometers, modern missions also incorporate broadband irradiance monitors such as SDO/EVE [39], which provide continuous full-disk spectral coverage essential for studies of solar-cycle variability and flare energetics. Together, these observational capabilities deliver a diverse set of temperature-, density-, and velocity-sensitive diagnostics, enabling reconstruction of plasma conditions across the chromosphere, transition region, and corona [1,2,40]. Increasingly, such datasets also serve as the foundation for machine-learning-based spectral classification and inversion techniques [41,42].

3.1 Space-Based UV and X-ray Spectrometers

Space-based UV and X-ray spectrometers have revolutionized solar atmospheric studies by providing access to wavelength regimes that are inaccessible from the ground due to atmospheric absorption [1,2,7]. These instruments offer the spectral, spatial, and temporal resolution required to resolve fine-scale dynamics, including chromospheric evaporation, transition-region explosive events, coronal upflows, and turbulent motions [3,35,37,38].

- **Hinode/EIS**: The EUV Imaging Spectrometer onboard *Hinode* performs high-resolution spectroscopy in the extreme ultraviolet (170–210 Å and 250–290 Å), targeting numerous coronal iron lines (Fe VIII–Fe XXIV). EIS enables precise measurements of line intensities, Doppler shifts, and non-thermal broadening, supporting diagnostics of coronal temperature, density, and plasma flows [16,38]. Its observations have revealed persistent upflows at active-region boundaries, dynamic coronal loops, and signatures of impulsive heating [37].

- **IRIS**: The Interface Region Imaging Spectrograph provides high-resolution UV spectroscopy and imaging of the chromosphere and transition region, observing key di-

agnostics such as Mg II h/k, C II, and Si IV. IRIS has been pivotal in identifying small-scale jets, explosive events, and pronounced line-profile asymmetries linked to reconnection and wave activity [3,12,17]. Its high temporal cadence, reaching ∼2 s in sit-and-stare mode, enables tracking of rapidly evolving phenomena [43].

- **SDO/EVE**: The EUV Variability Experiment aboard the Solar Dynamics Observatory provides continuous full-disk spectral irradiance measurements from 0.1 to 105 nm. EVE is central to studies of flare irradiance, solar-cycle variability, and global coronal heating, and provides essential context for high-resolution, localized observations [39,44].

- **Solar Orbiter/STIX and SPICE**: The STIX and SPICE instruments aboard *Solar Orbiter* deliver advanced X-ray and EUV diagnostics from varying heliocentric distances. STIX observes high-energy flare emission, enabling constraints on non-thermal electron distributions and flare energetics [18]. SPICE targets key transition-region and coronal lines (e.g., O VI, Ne VIII) with high spectral resolution, supporting studies of solar wind source regions and inter-instrument cross-calibration [36,45].

- **SOHO/SUMER**: The SUMER instrument onboard SOHO has played a foundational role in UV solar spectroscopy, covering the Lyman continuum and a wide range of transition-region lines [15]. SUMER provided early high-resolution measurements of Doppler shifts, non-thermal broadening, and spectral atlases that continue to underpin modern spectroscopic analyses [7,46].

Each instrument samples specific formation-temperature regimes, spanning from $\sim 10^4$ K in the chromosphere and lower transition region to $\sim 10^7$ K in flaring coronal plasma [1,3]. Their combined spectral, spatial, and temporal capabilities determine their sensitivity to plasma flows, wave motions, turbulence, and heating processes. Coordinated multi-instrument observations therefore enable comprehensive reconstruction of physical conditions from the lower atmosphere to the corona, forming the basis for both empirical diagnostics and physics-based modeling [2,41].

4 Physical Diagnostics from Spectral Lines

Spectral lines formed throughout the solar atmosphere constitute one of the most powerful and versatile tools for diagnosing plasma properties such as temperature, electron density, bulk flows, turbulence, elemental abundances, and ionization states [1,2,7]. In the UV, EUV, and X-ray wavelength ranges, numerous transitions of highly ionized species provide direct access to plasma conditions in the chromosphere, transition region, and corona, where magnetic and dynamic processes dominate energy transport and dissipation.

The formation of solar spectral lines is governed by a combination of collisional excitation, radiative decay, ionization and recombination processes, opacity effects, and departures from ionization or thermodynamic equilibrium [9,47]. In the low-density corona, optically thin conditions often prevail, allowing line intensities to be related directly to emission measures and atomic parameters. By contrast, chromospheric and some transition-region lines form under optically thick, non-LTE conditions and require full radiative-transfer modeling [5,48].

Modern atomic databases such as CHIANTI [25,49] and ADAS [50] provide the essential atomic data needed to compute emissivities, ionization balances, and synthetic spectra, forming the backbone of quantitative spectroscopic diagnostics. Below, we summarize the principal classes of physical diagnostics derived from UV and X-ray spectral lines.

4.1 Density Diagnostics

Electron density diagnostics are commonly based on ratios of spectral lines originating from metastable levels, whose populations depend sensitively on collisional excitation rates. Well-established examples include the Fe XII (186/195 Å), Fe XIII (203/202 Å), and O IV (1399/1401 Å) line pairs [2,35]. These ratios are only weakly dependent on temperature, making them robust diagnostics over a wide range of plasma conditions from the transition region to the corona.

Such density-sensitive ratios are routinely employed by spectrometers including Hinode/EIS, IRIS, SOHO/SUMER, and Solar Orbiter/SPICE to map electron densities in coronal loops, flare kernels, transition-region jets, and solar-wind source regions [37,43,51]. Figure 1 illustrates a schematic diagnostic curve for the Fe XII 186/195 Å ratio, which exhibits a characteristic monotonic increase with electron density due to enhanced collisional coupling of the relevant metastable levels. This behavior closely reflects that predicted by CHIANTI-based atomic models and observed in EUV spectroscopic measurements [2,35].

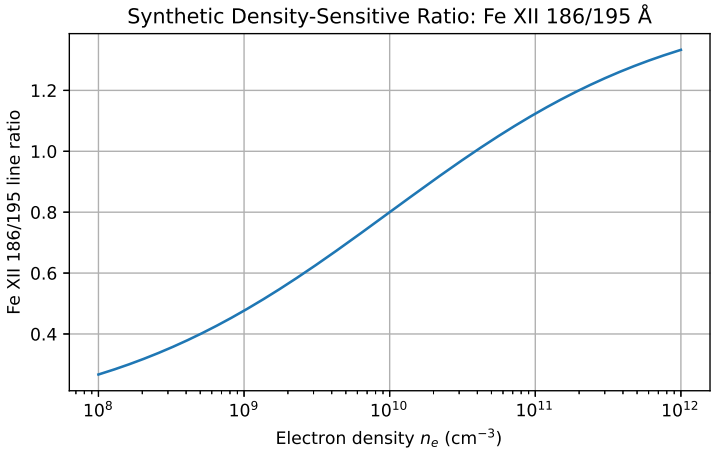

Figure 1: Synthetic density–sensitive diagnostic curve for the Fe XII 186/195 Å line ratio as a function of electron density. The monotonic rise of the ratio with n_e reflects the increasing collisional population of the metastable upper levels responsible for the 186 Å and 195 Å transitions. While this plot is schematic, it qualitatively reproduces the behavior predicted by atomic models such as CHIANTI and observed by space-based UV/EUV spectrometers including Hinode/EIS, IRIS, SUMER, and Solar Orbiter/SPICE [2,35,37,43,51]. Such density-sensitive ratios are routinely employed to diagnose plasma conditions in coronal loops, transition-region jets, flare footpoints, and solar-wind source regions.

At sufficiently high densities, such as those encountered in flare footpoints, line ratios may approach their high-density limits, necessitating alternative diagnostics including X-ray satellite lines or continuum emission [52]. Moreover, time-dependent simulations demonstrate that rapid heating can drive plasmas out of ionization equilibrium, modifying density-sensitive ratios during impulsive events [47].

4.2 Temperature Diagnostics

Temperature diagnostics rely primarily on two complementary approaches: temperature-sensitive line ratios and Differential Emission Measure (DEM) analysis. Ratios of lines from adjacent ionization stages (e.g., Fe XIV/Fe XII) provide localized temperature sensitivity and are well suited for quasi-isothermal structures such as coronal loops and bright points [53].

For multithermal plasmas, DEM inversion techniques reconstruct the distribution of emitting material as a function of temperature. Methods based on regularization, Bayesian inference, or sparse inversion are now widely applied to combined datasets from instruments such as AIA, EIS, XRT, and SPICE [21,54]. At flare temperatures exceeding $\sim$10 MK, strong emission from highly ionized iron (Fe XXIII–Fe XXVI), together with bremsstrahlung continua and Fe K-shell features near 6.7 keV, enables robust temperature diagnostics using X-ray spectroscopy [55].

4.3 Velocity and Flow Diagnostics

Doppler shifts of spectral lines provide direct measurements of plasma motions along the line of sight. Transition-region lines observed by IRIS, such as Si IV 1402 Å, frequently exhibit rapid and spatially localized redshifts and blueshifts associated with reconnection outflows, spicules, explosive events, and chromospheric evaporation [17,56].

In contrast to these highly dynamic phenomena, the quiet Sun provides an essential reference for average plasma flows. Using SOHO/SUMER observations, [57] measured systematic Doppler shifts of coronal lines formed up to $\sim$2 MK, finding small redshifts in transition-region lines and near-zero to weak blueshifts in coronal lines. These results indicate a smooth, temperature-dependent transition from downflows to upflows and place important constraints on mass circulation between the lower atmosphere and the corona.

In active regions, Hinode/EIS observations reveal persistent upflows with velocities of 5–30 $\mathrm{km\,s^{-1}}$ at active-region boundaries, widely interpreted as contributors to the slow solar wind [51]. During flares, evaporation flows observed in hot lines such as Fe XXI can exceed 200 $\mathrm{km\,s^{-1}}$, reflecting rapid energy deposition and mass transport into the upper corona.

Figure 2 shows full-Sun Doppler diagnostics derived from EUV spectroscopy, illustrating large-scale flow patterns in the Fe XIII 202.044 Å line [58]. In addition to bulk flows, excess line widths beyond thermal expectations provide evidence for unresolved motions, turbulence, and wave activity, offering insight into the role of small-scale dynamics in coronal heating [59].

4.4 Ionization and Non-Equilibrium Diagnostics

Many spectroscopic diagnostics assume ionization equilibrium; however, rapid heating or cooling can drive plasmas into non-equilibrium states where ionization and recombination timescales become significant [60]. Observable signatures include anomalous line ratios, delayed emission from high-charge states, and discrepancies between inferred temperatures and ion populations [9]. Such effects are particularly important in flares, nanoflares, and highly dynamic transition-region structures.

Charge-state distributions inferred from UV and EUV spectroscopy, together with in-situ solar-wind measurements, provide valuable constraints on heating rates and plasma expansion histories [61,62].

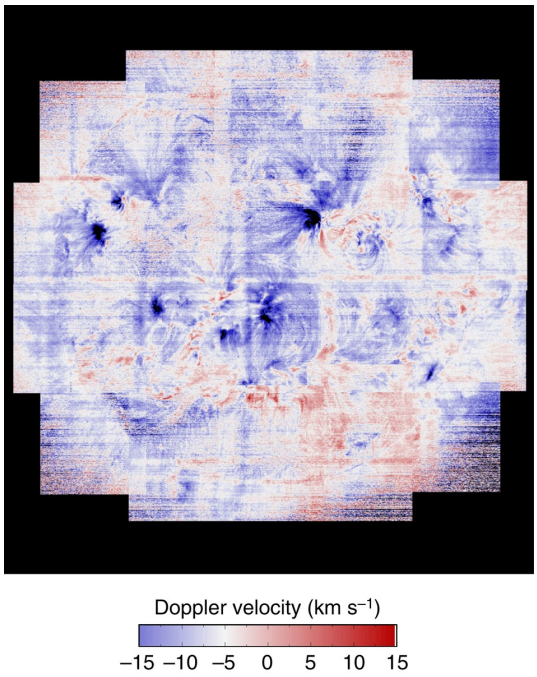

Figure 2: Full-Sun maps of Doppler shift and line width for the Fe XIII 202.044 Å line, illustrating large-scale velocity and flow diagnostics in the solar corona. The Doppler velocity map reveals widespread blueshifted regions at active-region boundaries and coronal hole interfaces, indicative of persistent coronal upflows. Redshifted and near-zero velocity regions correspond predominantly to closed magnetic structures [58].

4.5 Abundance Diagnostics

Elemental abundances are commonly diagnosed using ratios of lines from low first-ionization-potential (FIP) elements (e.g., Fe, Si, Mg) relative to high-FIP elements (e.g., O, Ne, S), with careful control of temperature and density effects. These measurements reveal the FIP effect, whereby low-FIP elements are preferentially enhanced in the corona relative to photospheric abundances [63,64].

The magnitude of the FIP bias varies with magnetic topology and solar environment, with closed magnetic structures typically exhibiting strong enhancement and open-field regions showing near-photospheric composition [65]. Spectroscopic observations from SUMER, EIS, and SPICE enable spatially resolved abundance mapping, providing crucial links between coronal heating, magnetic connectivity, and the sources of the solar wind.

5 Symmetry and Asymmetry in Solar Spectral Lines

The symmetry properties of solar spectral lines constitute a sensitive diagnostic of plasma dynamics, energy release, and radiative-transfer effects throughout the solar atmosphere. In an idealized, static, optically thin plasma with Maxwellian velocity distributions, emission lines are expected to exhibit symmetric, approximately Gaussian profiles determined by the combined effects of thermal and non-thermal broadening [1,2]. However, high-resolution observations from SOHO/SUMER, Hinode/EIS, IRIS, and Solar Orbiter/SPICE demon-

strate that many ultraviolet and X-ray lines depart significantly from this idealized behavior [3,17,66]. Such deviations often manifest as asymmetric profiles or enhanced wings, reflecting unresolved flows, multi-thermal plasma components, impulsive heating, and wave–particle interactions [67,68].

5.1 Blue-Wing Enhancements

Enhancements in the blue wings of spectral lines are commonly observed in coronal and transition-region diagnostics such as Fe XII, Fe XIII, Si IV, and C IV. Persistent blue-wing asymmetries detected at active-region boundaries have been interpreted as signatures of upward-directed plasma flows with velocities of several to tens of $\mathrm{km\,s^{-1}}$, potentially contributing to the slow solar wind [51,69]. IRIS observations further reveal intermittent, high-velocity blue-wing excursions (up to $\sim$150 $\mathrm{km\,s^{-1}}$) associated with impulsive heating events and nanoflare-driven chromospheric evaporation [12,70]. These phenomena frequently produce non-Gaussian line wings that cannot be captured by single-component fits and instead require multi-component or asymmetric profile modeling [3,71].

5.2 Red-Wing Excess

Red-wing asymmetries arise from plasma motions directed toward the solar surface and are commonly linked to condensation, cooling, and downflow processes. Transition-region lines such as Si IV and O IV often exhibit impulsive redshifts during the early cooling phases of flares, consistent with downward reconnection outflows and chromospheric condensation [43, 72]. Hydrodynamic flare models predict that rapid energy deposition drives strong downflows in the lower atmosphere, producing pronounced red-wing excesses on timescales of seconds to minutes [73,74]. On larger spatial scales, systematic redward asymmetries observed in post-flare loops and coronal rain reflect gravitationally driven plasma drainage and cooling along magnetic field lines [75,76].

5.3 Multi-Component Gaussian Structure

A substantial fraction of observed solar spectral lines cannot be adequately described by a single Gaussian component. Instead, two or more Gaussian components are often required, representing a superposition of quasi-static background emission and dynamically evolving plasma along the line of sight [3,77]. Common examples include a narrow, near-rest component combined with a broad, high-velocity wing in IRIS Si IV spectra, multiple Fe XII components in Hinode/EIS observations of active-region outflows, and multi-temperature components in flare-related Fe XXI and Fe XXIV lines. Such multi-component structures provide strong evidence for fine-scale reconnection jets, intermittent heating, and turbulent plasma motions in the corona [21,78].

5.4 Opacity-Induced Asymmetry

In optically thick chromospheric lines, including Mg II h/k, Hα, and Ca II 8542 Å, line asymmetries are frequently dominated by radiative-transfer effects rather than simple kinematics. Strong gradients in opacity and source function with height lead to asymmetric profiles that are highly sensitive to atmospheric velocity gradients, shock propagation, temperature inhomogeneities, and partial frequency redistribution (PRD) effects [26,48]. Radiation–hydrodynamic simulations using models such as RADYN and Bifrost demonstrate that

the observed asymmetries in Mg II lines are closely linked to steep vertical flows and non-equilibrium ionization in the dynamic chromosphere [5,26].

6 Broadening Mechanisms

As discussed in the previous sections, both the symmetry properties and Doppler shifts of solar spectral lines encode key information on plasma flows and dynamics. Complementary to these diagnostics, the width of spectral lines provides one of the most powerful probes of plasma conditions in the solar atmosphere, carrying information on temperature, unresolved motions, turbulence, magnetic fields, radiative-transfer effects, and instrumental limitations. In an idealized, static, optically thin plasma, line widths are determined solely by thermal Doppler broadening. Solar observations, however, consistently reveal widths exceeding the thermal expectation, indicating the presence of additional physical processes acting over a wide range of spatial and temporal scales [1,3,7].

The solar atmosphere spans extreme physical regimes, with temperatures ranging from $\sim 10^4$ K in the chromosphere to $\sim 10^7$ K in flares, and magnetic field strengths varying from a few gauss in the quiet corona to kilogauss values in photospheric active-region concentrations. As a consequence, multiple broadening mechanisms often operate simultaneously along the line of sight. Disentangling their respective contributions is therefore essential for deriving physically meaningful diagnostics, including non-thermal velocities, microturbulence, ion temperature anisotropies, flare energetics, and transition-region dynamics [79,80]. Figure 3 schematically illustrates how these different mechanisms contribute to the observed line profile.

High-resolution UV and X-ray spectra obtained by SOHO/SUMER, Hinode/EIS, IRIS, and Solar Orbiter/SPICE and STIX routinely show excess broadening beyond the thermal Doppler width. Such excess widths are commonly interpreted as signatures of unresolved Alfvénic waves, turbulent motions, nanoflare-driven flows, or reconnection outflows [43,71, 81]. Under flare conditions, strong broadening is observed in high-temperature EUV and X-ray lines, reflecting the coexistence of hot thermal ion populations and highly non-thermal particle distributions [1].

The observed spectral line width $\Delta\lambda_{\rm obs}$ is commonly modeled as the quadratic sum of several independent contributions:

$$\Delta\lambda^2_{\rm obs} = \Delta\lambda^2_{\rm th} + \Delta\lambda^2_{\rm nth} + \Delta\lambda^2_{B} + \Delta\lambda^2_{\rm Stark} + \Delta\lambda^2_{\rm op} + \Delta\lambda^2_{\rm inst}, \tag{1}$$

where the individual terms represent thermal, non-thermal (turbulent), magnetic (Zeeman), Stark, opacity-related, and instrumental broadening, respectively, as visualized in Fig. 3. Although this decomposition is widely adopted, it relies on assumptions of statistical independence and near-Gaussian velocity distributions that may break down in highly dynamic or optically thick environments [80,82]. Accurate separation of these contributions is therefore critical in studies of coronal heating, wave–particle interactions, and energy transport, where non-thermal widths are often interpreted as evidence of unresolved dissipation processes.

6.1 Thermal Broadening

Thermal broadening (green curve in Fig. 3) arises from the Maxwellian velocity distribution of emitting ions in a plasma at temperature T. The line-of-sight component of the ion

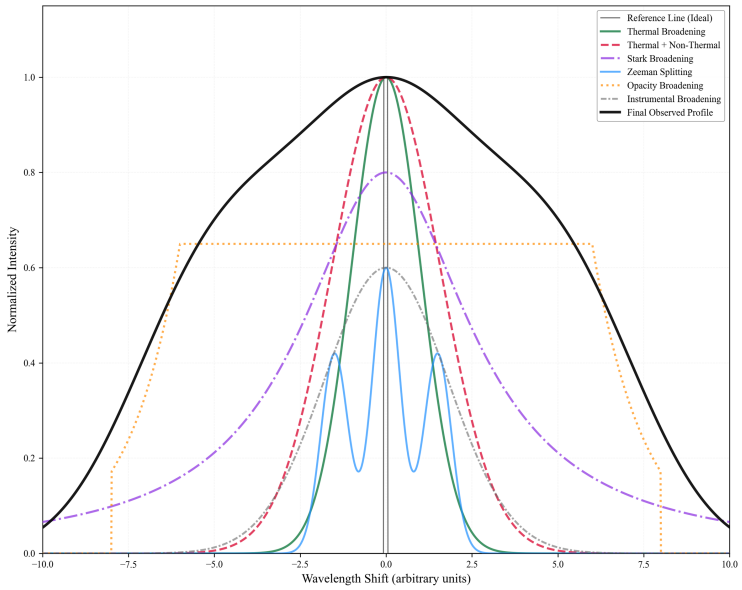

Figure 3: Schematic illustration of spectral line broadening mechanisms in the solar atmosphere. The thin black reference line represents an ideal, unbroadened spectral line. Successive broadening mechanisms are shown: thermal Doppler broadening (green Gaussian), combined thermal and non-thermal turbulent broadening (red dashed Gaussian), Stark broadening due to electric microfields (purple dash-dot Lorentzian), Zeeman splitting from magnetic fields (blue triple Gaussian), opacity broadening from optically thick effects (orange dotted profile), and instrumental broadening (gray dash-dot-dot). The thick black curve shows the final observed profile resulting from the combined effects.

velocity produces Doppler shifts that result in a Gaussian line profile with a width given by

$$\Delta\lambda_{\mathrm{th}} = \lambda_0 \sqrt{\frac{2kT}{mc^2}}, \tag{2}$$

where m is the ion mass and λ_0 the rest wavelength. This expression assumes ion–electron thermal equilibrium and isotropic velocity distributions.

In the solar corona, typical temperatures of $T \sim 1$–$3\,\mathrm{MK}$ correspond to thermal velocities of heavy ions such as Fe XII, Fe XIV, and Fe XV of order 20–30 $\mathrm{km\,s^{-1}}$, yielding relatively narrow Doppler widths compared to those commonly observed [2,7]. Because the thermal width scales as $m^{-1/2}$, lighter ions (e.g., O, C, and Si) exhibit broader thermal profiles than heavier ions formed at similar temperatures, providing a direct diagnostic of ion temperature and mass-dependent heating.

In many coronal and transition-region observations, measured line widths substantially exceed the expected thermal contribution, indicating the presence of additional non-thermal broadening mechanisms. Reliable estimation of the thermal component is therefore a prerequisite for isolating non-thermal velocities associated with waves, turbulence, or unresolved bulk flows. Comparisons of line widths across ions with different masses are frequently employed to discriminate between wave-driven heating scenarios and impulsive energy release processes such as nanoflares [3,71].

6.2 Non-Thermal (Turbulent) Broadening

Non-thermal broadening (red dashed curve in Fig. 3) reflects unresolved motions caused by turbulence, Alfvénic waves, microjets, or multi-threaded flows [11,43,82]. It is commonly parameterized by a non-thermal velocity $\xi_{\rm nth}$,

$$\Delta\lambda_{\rm nth} = \frac{\lambda_0 \xi_{\rm nth}}{c}. \tag{3}$$

IRIS observations indicate that transition-region lines such as Si IV and Mg II h/k typically exhibit $\xi_{\rm nth}$ values of 10–25 $\mathrm{km\,s^{-1}}$ in active regions [71,81]. During flares, non-thermal velocities can exceed 50–100 $\mathrm{km\,s^{-1}}$, consistent with reconnection-driven turbulence and wave generation [83,84]. These measurements provide important constraints on models of wave dissipation and turbulence-driven coronal heating.

6.3 Stark Broadening

Stark broadening (purple dash-dot curve in Fig. 3) arises from electric microfields generated by nearby electrons and ions and becomes significant in high-density environments such as flare kernels, chromospheric condensations, and post-flare loops, where electron densities exceed $10^{12}\,\mathrm{cm^{-3}}$ [85,86]. Although most EUV and X-ray coronal lines are formed under conditions where Stark broadening is negligible, certain flare-related lines (e.g., Fe XXI 1354 Å) can exhibit measurable Stark wings. Stark effects are also essential for modeling hydrogen Balmer and Lyman lines during flare impulsive phases [87].

6.4 Zeeman Splitting

Magnetic broadening due to the Zeeman effect (blue curve in Fig. 3) depends on the Landé factor g and the magnetic field strength B,

$$\Delta\lambda_B = 4.67 \times 10^{-13}\, g\, \lambda_0^2 B. \tag{4}$$

Zeeman splitting is most readily observed in photospheric lines, but detectable signatures also appear in chromospheric and transition-region lines through spectropolarimetric measurements [88,89]. In the corona, the effect is generally weak, although future facilities such as DKIST and Solar Orbiter/Metis aim to extend magnetic diagnostics to infrared and UV coronal lines [90].

6.5 Opacity Broadening

Opacity-related broadening (orange dotted curve in Fig. 3) occurs when spectral lines are partially or fully optically thick, leading to multiple scattering and radiative-transfer-induced profile modifications. Such effects can produce non-Gaussian wings, core reversals, and asymmetries in lines such as Mg II h/k, C II, and Hα [26,48]. IRIS observations demonstrate that opacity broadening plays a central role in interpreting chromospheric heating events and reconnection-driven jets [91]. Accurate separation of thermal and opacity contributions generally requires detailed radiative-transfer modeling using tools such as RH or radiation–MHD simulations.

6.6 Instrumental Broadening

All spectroscopic measurements are convolved with the instrumental line-spread function (LSF) (gray curve in Fig. 3), which must be accurately characterized to recover intrinsic line widths. For example, the Hinode/EIS LSF varies across the detector and requires careful calibration [13], while the spectral resolution of IRIS ($\sim$ 26–53 mÅ) introduces a non-negligible contribution to the observed widths of narrow chromospheric lines [17]. Similarly, SUMER exhibited a well-characterized Gaussian LSF but required corrections for instrumental degradation over its mission lifetime [46].

Failure to account for instrumental broadening can lead to systematic overestimates of non-thermal velocities by 20–50% [7,92]. Precise instrumental calibration is therefore essential for flare studies and for quantifying small-amplitude wave motions in the corona.

The simultaneous action of multiple broadening mechanisms, together with plasma flows and line-profile asymmetries discussed in the preceding sections, implies that the observed solar spectral lines often deviate from simple, idealized shapes. In many cases, the measured profiles cannot be uniquely interpreted in terms of a single physical process, as thermal, non-thermal, opacity-related, and instrumental effects are intrinsically entangled along the line of sight.

As a result, quantitative interpretation of spectral line widths, Doppler shifts, and asymmetries requires explicit modeling of the full line profile rather than reliance on single diagnostic parameters. This necessity has motivated the development and widespread use of profile analysis techniques based on parametric representations—such as Gaussian, Lorentzian, Voigt, and multi-component models—as well as more advanced fitting and decomposition approaches tailored to different physical regimes of the solar atmosphere [2,3,66].

In the following section, we review the most commonly employed methods for spectral line profile analysis in solar physics, with emphasis on their physical assumptions, diagnostic capabilities, and limitations when applied to high-resolution UV and X-ray observations.

7 Methods for Spectral Line Profile Analysis

Quantitative interpretation of solar spectral lines requires a precise mathematical description of the observed intensity profile $I(\lambda)$. While an idealized, static plasma would produce symmetric Gaussian profiles, solar observations often show significant deviations due to the combined effects of thermal motions, unresolved flows, turbulence, opacity, and instrumental broadening.

To account for these complexities, a variety of profile-analysis methods have been developed. These range from simple single-Gaussian fits to multi-component, asymmetric, or composite models, each designed to capture different physical aspects of the observed line shapes in UV and EUV spectra [2,3,66,93,94].

7.1 Single-Gaussian Line Profile

The simplest and most widely used approach assumes that the observed intensity can be represented by a single Gaussian:

$$I(\lambda) = I_0 \exp\left[-\frac{(\lambda - \lambda_c)^2}{2\sigma^2}\right] + B, \tag{5}$$

where I_0 is the peak intensity, λ_c the centroid, σ the Gaussian width, and B a constant background.

The line-of-sight Doppler velocity is then

$$v_{\rm Dop} = c\frac{\lambda_c - \lambda_0}{\lambda_0}, \tag{6}$$

and the total velocity width is

$$\xi_{\rm tot} = \frac{c\,\sigma}{\lambda_0}, \tag{7}$$

which includes thermal, non-thermal, and instrumental contributions unless explicitly removed.

Single-Gaussian fitting is computationally efficient and forms the backbone of many large-scale analyses with instruments such as SOHO/SUMER, Hinode/EIS, and IRIS. However, this approach assumes a single homogeneous plasma component and may fail to capture weak high-velocity wings, asymmetries, or multiple flow components [3,66,93–95].

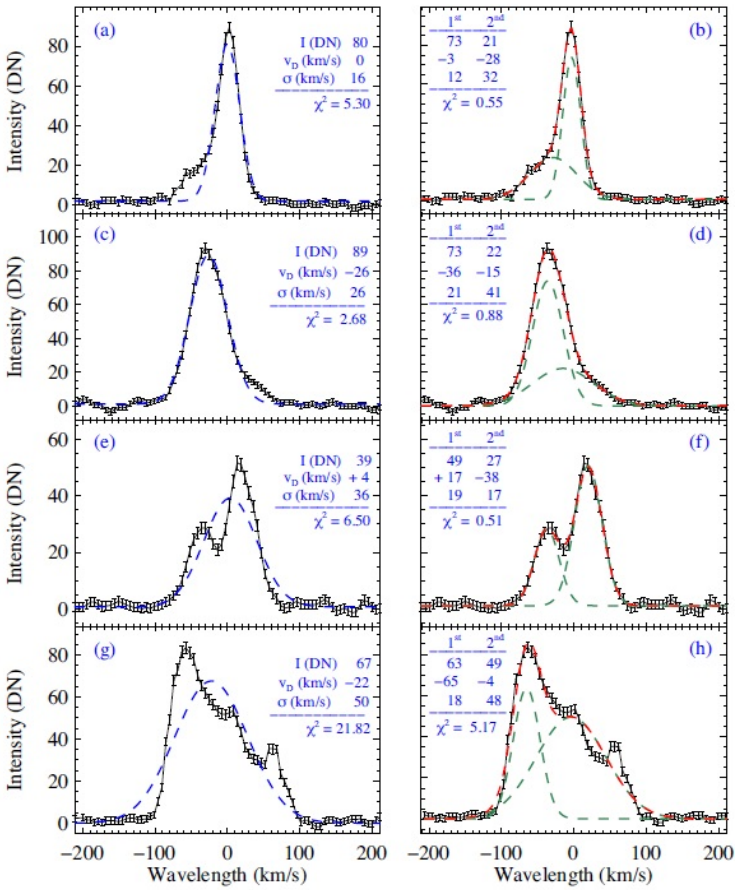

Figure 4: Comparison of single- and double-Gaussian fits to observed line profiles. Blueward asymmetries (panels a,b) and redward asymmetries (panels c,d) are shown, along with double-peak (panels e,f) and complex multi-peak profiles (panels g,h). The peak intensity I, Doppler velocity v_D, and width σ are indicated in DN and km s^{-1} [93].

7.2 Multi-Gaussian Decomposition

To represent asymmetric or multi-component emission, the observed intensity can be written as a sum of N Gaussians:

$$I(\lambda) = \sum_{i=1}^{N} I_i \exp\left[-\frac{(\lambda - \lambda_{c,i})^2}{2\sigma_i^2}\right] + B, \tag{8}$$

where each component has its own I_i, $\lambda_{c,i}$, and σ_i.

In practice, $N = 2$ is commonly used, corresponding to a narrow core and a broader, shifted wing component. This decomposition effectively isolates weak, high-velocity flows in coronal and transition-region lines such as Fe XII, Fe XIII, and Si IV [3,51,66,93–95]. Figure 4 illustrates how multi-Gaussian fits better capture asymmetries and extended wings than single-Gaussian fits.

Multi-Gaussian fitting improves the characterization of dynamic plasma components, even when secondary components contribute a small fraction of the total intensity [94]. However, the method introduces additional free parameters, increasing the risk of degeneracy. Robust interpretation therefore requires additional constraints, such as spatial coherence, temporal evolution, or complementary diagnostics [2].

7.3 Lorentzian Profile Fitting

Lorentzian profiles, characterized by

$$L(\lambda) = I_0 \frac{\gamma^2}{(\lambda - \lambda_0)^2 + \gamma^2}, \tag{9}$$

arise from radiative damping or pressure broadening. They produce broad wings that can represent high-density or highly dynamic regions, including flare kernels [1,96].

In most UV/EUV lines, Doppler broadening dominates, so Lorentzian fits are typically used phenomenologically or as components in composite profiles such as Voigt functions [2,3]. Their physical interpretation in terms of thermal or non-thermal velocities is limited.

7.4 Voigt Profile Representation

When both Doppler and damping effects are important, the line profile can be represented by a Voigt function:

$$I(\lambda) = I_0\, V(\lambda - \lambda_c; \sigma, \gamma) + B, \tag{10}$$

where σ and γ are the Gaussian and Lorentzian widths, respectively.

Voigt profiles are relevant for optically thick chromospheric lines or flare spectra where damping contributes [1]. They provide a compact description of non-Gaussian features such as enhanced wings or peaked cores, though the fitted parameters do not uniquely constrain the underlying physics and should be interpreted alongside complementary diagnostics or modeling [3,94].

7.5 Transition-Region Line Asymmetries and Bayesian Profile Modeling

Building on the multi-component and Voigt profile approaches described above, the solar transition region provides an ideal testbed for investigating line asymmetries caused by dynamic, multi-thermal plasma structures. Spectral lines formed in this layer are particularly

prone to asymmetries due to the coexistence of multiple plasma components along the line of sight and the highly dynamic nature of the atmosphere. High-resolution IRIS observations of the Si IV 1394 and 1403 Å lines reveal that these profiles frequently deviate from simple Gaussian shapes, exhibiting enhanced wings, skewness, and multi-component structures [94].

Using a Bayesian Markov Chain Monte Carlo (MCMC) framework, [94] systematically modeled Si IV line profiles across various solar environments, including flaring and non-flaring active regions, plage, coronal holes, and quiet-Sun boundaries. Their analysis shows that asymmetric profiles are common and often require double-Gaussian or Voigt representations to accurately capture the observed line shapes. Figure 5 (adapted from [94]) illustrates representative redward asymmetric profiles in flaring active regions, where a single-Gaussian fit systematically underestimates the line wings, while a double-Gaussian model successfully separates a dominant core from a secondary redshifted component. Model performance was evaluated using several statistical measures: the reduced chi-squared (χ^2), Akaike Information Criterion (AIC), and Bayesian Information Criterion (BIC).

Blue-wing asymmetries are equally prominent in transition-region spectra. Figure 6 (adapted from [94]) presents a clear example of a Si IV 1394 Å profile with a pronounced blueward enhancement, where Bayesian model comparison based on AIC and BIC strongly favors a double-Gaussian description. Such blueward secondary components are commonly interpreted as signatures of upward-directed flows, reconnection-driven jets, or impulsive heating events producing high-velocity plasma motions unresolved by imaging alone.

A key methodological advance of [94] is the incorporation of non-Gaussian intensity uncertainties into the likelihood function, motivated by observed deviations of IRIS measurement errors from normal distributions. By introducing an additional parameter to quantify departures from Gaussian noise and employing an affine-invariant ensemble MCMC sampler, the authors obtained robust posterior distributions for line parameters, including centroid shifts, widths, and relative amplitudes of multiple components. This probabilistic approach allows reliable identification of weak secondary components responsible for spectral asymmetries, even when traditional least-squares fitting fails.

Overall, the results of [94] demonstrate that asymmetries in transition-region lines are not merely fitting artifacts but encode essential information about unresolved plasma dynamics. When combined with rigorous Bayesian model selection and uncertainty quantification, spectral asymmetry analysis emerges as a powerful diagnostic of heating, reconnection, and multi-thermal structuring in the solar transition region.

8 Discussion

Over the past decades, solar spectroscopy has undergone a transformative evolution, transitioning from manual line identification with early UV and X-ray instruments to highly automated and physics-informed analysis pipelines capable of processing high-resolution datasets from instruments such as Hinode/EIS, IRIS, Solar Orbiter, and DKIST [16,17,19,97].

This progress has been fueled by the synergy between advanced instrumentation, detailed radiative-transfer modeling (including non-LTE, non-equilibrium ionization, and multi-fluid approaches [26,98]), large atomic databases (e.g., CHIANTI [49]), and machine-learning frameworks [99,100]. Together, these tools enable comprehensive exploration of plasma dynamics across the solar atmosphere, from chromospheric heating and transition-region flows to coronal turbulence, reconnection, and flare energy release [3,7,94].

A significant area of advancement lies in understanding line asymmetries and broadenings. Multi-component and asymmetric profiles observed in transition-region lines, such as

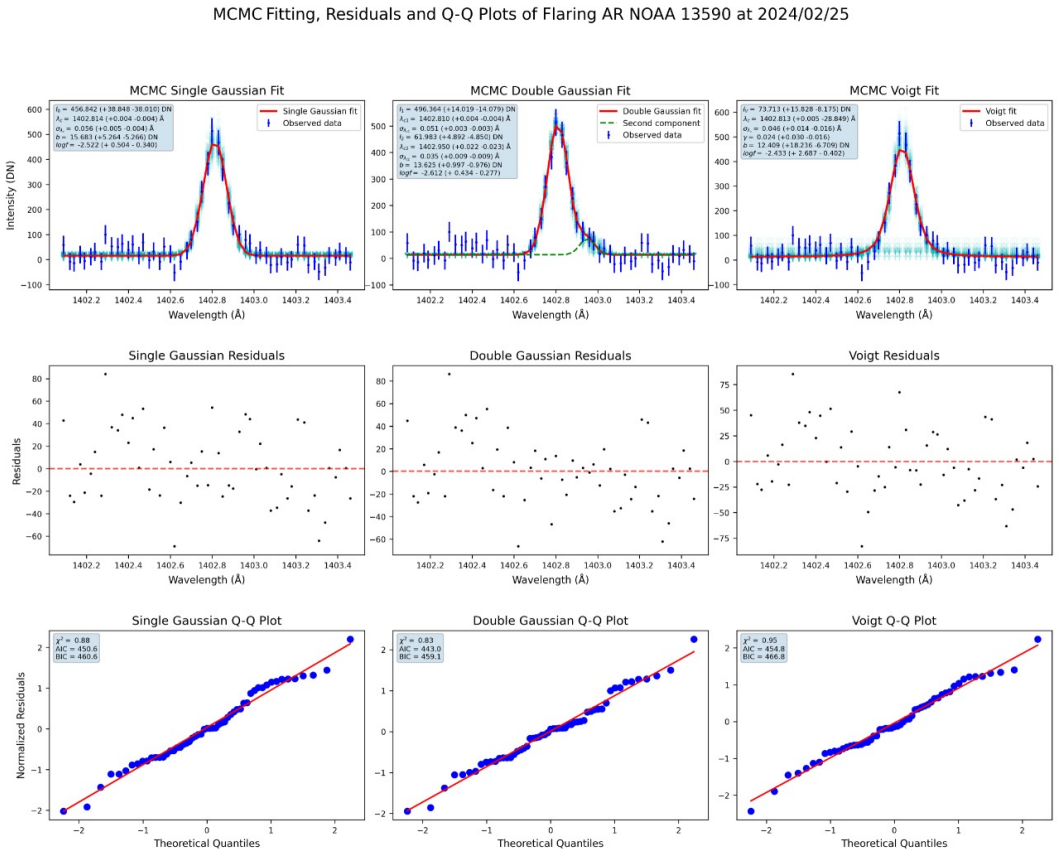

Figure 5: Bayesian MCMC fitting of the Si IV 1403 Å line profile for single-Gaussian (left), double-Gaussian (middle), and Voigt (right) models. Data observed by IRIS in flaring active region NOAA 13590 on 2024-02-25. Top: profile and MCMC models; middle: residuals; bottom: Q-Q plots. The blue shaded region shows the marginalized MCMC posterior. The double-Gaussian model outperforms both single-Gaussian and Voigt models. Model comparison statistics (χ^2, AIC, BIC) are shown [94].

Si IV 1394/1403 Å, reveal the coexistence of multiple plasma populations along the line of sight [94]. Bayesian MCMC modeling demonstrates that double-Gaussian or Voigt representations are often required to accurately capture both redward and blueward enhancements, providing robust constraints on unresolved flows, reconnection jets, and impulsive heating events (Figures 5 and 6). However, distinguishing among different physical origins of asymmetry—nanoflare-driven evaporation, spicule upflows, reconnection outflows, or opacity effects—remains challenging [71,101,102].

Instrumental effects also pose persistent limitations. Even modern spectrometers exhibit wavelength-dependent line-spread functions (LSFs) that can distort non-thermal widths or introduce artificial asymmetries [7,103]. Cross-instrument calibration between IRIS, EIS, SUMER, and Solar Orbiter remains essential for reliable comparison of line parameters and Doppler shifts, particularly in multi-thermal and high-cadence observations [104]. Accurate LSF deconvolution, together with uncertainty quantification through Bayesian or Monte Carlo methods, is crucial for distinguishing genuine plasma signatures from instrumental

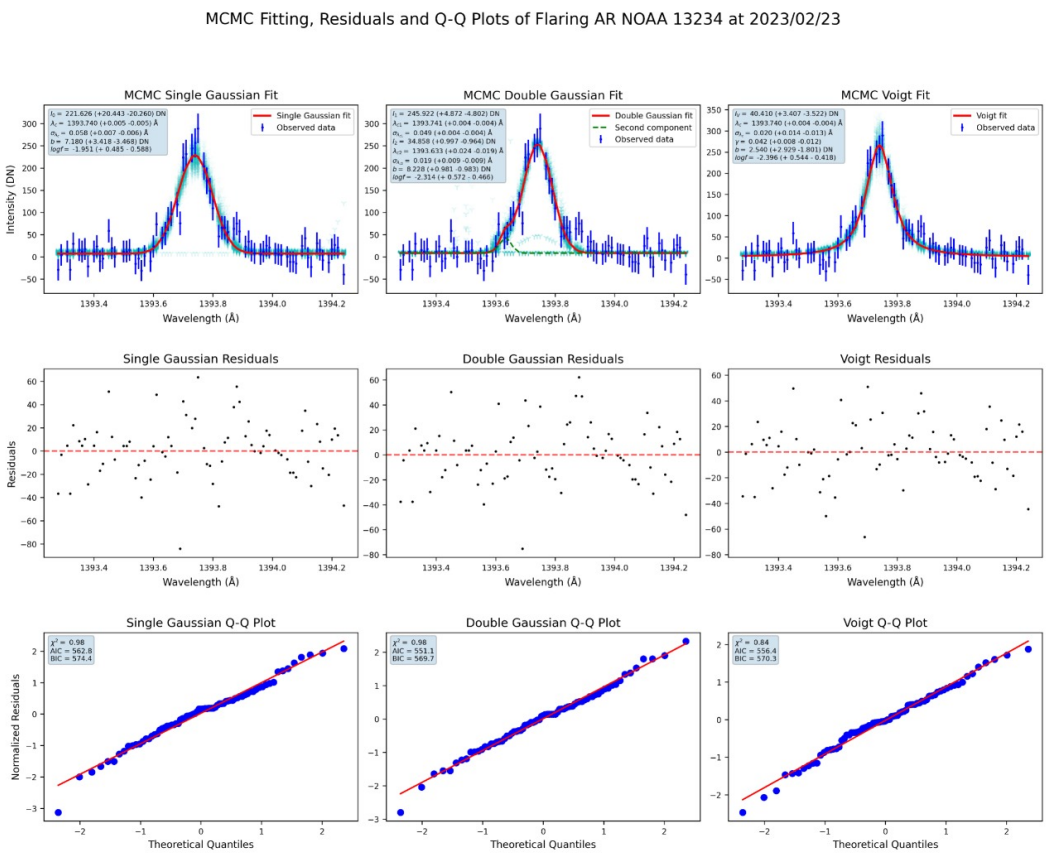

Figure 6: MCMC fitting of the Si IV 1394 Å line profile with blueward wing (IRIS, NOAA 13234, 2023-10-23) for single-Gaussian, double-Gaussian, and Voigt models. Top: profile and models with MCMC posterior (blue shading); middle: residuals; bottom: Q-Q plots [94].

artifacts.

The integration of machine-learning techniques with physics-based models offers promising pathways but introduces new challenges. Deep-learning approaches for DEM inversion, spectral fitting, or line classification can accelerate analysis but may violate physical constraints if not carefully constrained [21,105,106]. Hybrid frameworks combining PINNs, CHIANTI-based forward modeling, and uncertainty-aware inversion represent a viable strategy for extracting physically meaningful parameters from large, heterogeneous datasets.

Finally, coordinated multi-instrument observations are increasingly important. Combining data from Solar Orbiter, IRIS, DKIST, Hinode, and SDO enables simultaneous coverage across temperatures from 10^4 to 10^7 K and facilitates cross-validation of density, temperature, and flow diagnostics [94,104]. Standardized calibration pipelines, consistent wavelength scales, and robust cross-instrument correction of Doppler offsets and instrumental broadening are prerequisites for fully exploiting these rich datasets.

In summary, current challenges and future directions in solar spectral analysis include:

- Deconvolving overlapping physical sources of asymmetry, including multi-component flows, turbulence, and wave-particle interactions.

- Correcting for instrument-specific LSF effects and maintaining calibration over long-duration missions.
- Integrating physics-informed machine learning with radiative-transfer modeling to ensure physically consistent inversions.
- Establishing standardized cross-platform spectral calibration frameworks to unify multi-instrument datasets.

Addressing these challenges will advance our understanding of plasma dynamics, energy transport, and heating processes in the solar atmosphere.

8.1 Outlook and Future Challenges

Although solar spectroscopic diagnostics have advanced substantially in recent years, important challenges persist in the quantitative interpretation of increasingly complex spectral line profiles. Accurate determinations of Doppler shifts, line widths, and profile asymmetries remain strongly dependent on careful instrumental calibration, a precise knowledge of line spread functions, and consistent analysis across different instruments. These aspects become especially critical for coordinated, multi-instrument observations, where even modest differences in spectral resolution or sensitivity can lead to systematic biases in the inferred plasma properties.

At the same time, the rapidly expanding volume and complexity of high-resolution spectroscopic data demand analysis strategies that go beyond traditional fitting approaches. Within this landscape, machine-learning techniques are increasingly being explored as complementary tools for tasks such as automated profile classification, anomaly detection, and the acceleration of forward modeling and inversion schemes. When guided by physical insight and trained on realistic data, these methods offer a promising way to efficiently probe large parameter spaces while maintaining a transparent connection to the underlying plasma physics.

Looking forward, closer integration of physics-informed machine-learning frameworks with established spectroscopic diagnostics and radiative-transfer modeling is expected to become an important component of future analysis pipelines. Combined with coordinated observations from facilities such as IRIS, Solar Orbiter, and DKIST, and supported by robust statistical inference and hybrid methodologies, these developments are likely to provide deeper insight into plasma heating, magnetic reconnection, and energy transport throughout the solar atmosphere.

9 Conclusion

Solar spectroscopy remains a cornerstone of heliophysics, offering unique insights into the thermal, magnetic, and dynamic properties of the solar atmosphere. Through careful analysis of spectral-line intensities, widths, asymmetries, and multi-component structures, researchers can probe a wide range of physical processes, including chromospheric heating, transition-region flows, coronal turbulence, magnetic reconnection, and flare energetics [1,3,7,94].

This review has synthesized observational, theoretical, and methodological advances in UV and X-ray spectroscopy. We highlighted key instruments, diagnostic techniques, and physical mechanisms governing line symmetry, asymmetry, and broadening—thermal, non-thermal, magnetic, opacity-driven, and instrumental. We also emphasized the role of modern

Bayesian and machine-learning frameworks in quantifying uncertainties and revealing subtle multi-component features, which complement traditional radiative-transfer and atomic-physics-based diagnostics.

Looking forward, next-generation observatories—including Solar Orbiter, IRIS 2.0, and DKIST—combined with physics-informed ML, high-cadence multi-wavelength observations, and advanced numerical simulations, promise unprecedented spectral coverage and diagnostic precision. These advances are expected to deepen our understanding of plasma heating, energy transport, magnetic reconnection, and the multi-scale dynamics of the Sun, ultimately improving space-weather forecasting and our broader knowledge of heliospheric physics.

In conclusion, solar spectral analysis continues to provide a critical bridge between high-resolution observations, physical modeling, and theoretical understanding, and it will remain central to unraveling the complex, multi-thermal, and dynamic nature of the solar atmosphere.

Authors' Contributions

All authors have the same contribution.

Data Availability

No data available.

Conflicts of Interest

The authors declare that there is no conflict of interest.

Ethical Considerations

The authors have diligently addressed ethical concerns, such as informed consent, plagiarism, data fabrication, misconduct, falsification, double publication, redundancy, submission, and other related matters.

Funding

This research did not receive any grant from funding agencies in the public, commercial, or nonprofit sectors.

References

[1] Phillips, K. J. H., Feldman, U., & Landi, E. 2008, Ultraviolet and X-ray Spectroscopy of the Solar Atmosphere, Cambridge University Press.

[2] Del Zanna, G., & Mason, H. E. 2018, Living Reviews in Sol. Phys., 15, 5.

[3] Peter, H. 2010, A&A, 518, A51.

[4] Asplund, M. e. a. 2000, A&A, 359, 729.

[5] Carlsson, M., & Stein, R. F. 1997, ApJ, 481, 500.

[6] Rutten, R. J. 2019, Living Reviews in Sol. Phys.,

[7] Del Zanna, G., & Mason, H. E. 2018, Living Reviews in Sol. Phys., 15, 5.

[8] Doschek, G. A., & Warren, H. P. 2016, ApJ, 825, 36.

[9] Reale, F. 2014, Living Reviews in Sol. Phys., 11, 4.

[10] Dzifčáková, E. e. a. 2015, ApJS, 213, 2.

[11] De Pontieu, B. e. a. 2007, Science, 318, 1574.

[12] Testa, P. e. a. 2014, Science, 346, 1255724.

[13] Young, P. R. e. a. 2018, ApJ.

[14] Culhane, J. L. e. a. 1991, Sol. Phys., 136, 89.

[15] Wilhelm, K. e. a. 1995, Sol. Phys., 162, 189.

[16] Culhane, J. L. e. a. 2007, Sol. Phys., 243, 19.

[17] De Pontieu, B. e. a. 2014, Sol. Phys., 289, 2733.

[18] Krucker, S. e. a. 2020, A&A, 642, A15.

[19] Rochus, P., et al. 2020, A&A, 642, A8.

[20] Kuridze, D., et al. 2021, J. Physics: Conference Series.

[21] Cheung, M. C. M. e. a. 2019, Nature Astronomy, 3, 160.

[22] Asensio Ramos, A., & Díaz Baso, C. J. 2019, A&A, 626, A102.

[23] Sainz Dalda, A., de la Cruz Rodriguez, J., De Pontieu, B., & Gosic, M. 2019, ApJ, 875, L18.

[24] Cheung, M. C. M., et al. 2019, ApJ, 882, 13.

[25] Dere, K. P., et al. 1997, A&AS, 125, 149.

[26] Leenaarts, J. e. a. 2013, ApJ, 772, 89.

[27] Rathore, B., Carlsson, M., & Leenaarts, J. 2015, ApJ, 811, 81.

[28] Landi Degl'Innocenti, E., & Landolfi, M. 2004, Polarization in Spectral Lines, Kluwer Academic Publishers.

[29] Teriaca, L., et al. 2012, A&A, 548, A28.

[30] Peter, H., et al. 2014, Science, 346, 1255726.

[31] Klimchuk, J. A. 2015, Philosophical Transactions of the Royal Society A, 373, 20140256.

[32] Del Zanna, G., et al. 2015, A&A, 582, A56.

[33] Gudiksen, B. V., et al. 2011, A&A, 531, A154.

[34] Allred, J., et al. 2015, ApJ, 809, 104.

[35] Young, P. R. 2021, Frontiers in Astronomy and Space Sciences, 8, 662790.

[36] Müller, D., et al. 2020, A&A, 642, A1.

[37] Doschek, G. A., et al. 2012, ApJ, 750, 22.

[38] Brooks, D. H., & Warren, H. P. 2016, ApJ, 820, 63.

[39] Woods, T. N., et al. 2012, Sol. Phys., 275, 115.

[40] Kuridze, D., et al. 2021, J. Physics: Conference Series.

[41] Testa, P., et al. 2021, Frontiers in Astronomy and Space Sciences, 8, 662790.

[42] Liu, L., et al. 2020, ApJ, 894, 70.

[43] Tian, H., et al. 2014, ApJ, 790, L29.

[44] Chamberlin, P. C., et al. 2009, Sol. Phys., 256, 255.

[45] Del Zanna, G. 2021, A&A.

[46] Curdt, W., et al. 2001, A&A, 375, 591.

[47] Bradshaw, S., & Mason, H. 2009, ApJ, 699, 1362.

[48] Rutten, R. 2003, Radiative transfer in stellar atmospheres.

[49] Dere, K. e. a. 2019, ApJS, 241, 22.

[50] Summers, H. 2004, Culham Laboratory Report.

[51] Brooks, D., & Warren, H. 2011, ApJ, 727, L13.

[52] Phillips, K. 2004, Advances in Space Research, 34, 410.

[53] Warren, H. e. a. 2008, ApJ, 677, 1395.

[54] Hannah, I. G., & Kontar, E. P. 2012, A&A, 539, A146.

[55] Holman, G. e. a. 2011, ApJ, 731, L52.

[56] Peter, H., & Judge, P. 1999, ApJ, 522, 1148.

[57] Dadashi, N., Teriaca, L., & Solanki, S. K. 2011, A&A, 534, A90.

[58] Brooks, D. H., Ugarte-Urra, I., & Warren, H. P. 2015, Nature Communications, 6, 5947.

[59] McIntosh, S. e. a. 2011, Nature, 475, 477.

[60] Bradshaw, S. e. a. 2006, A&A, 454, L41.

[61] Landi, E., & Miralles, M. 2012, ApJ, 744, 99.

[62] Boerner, P. e. a. 2014, Sol. Phys., 289, 2377.

[63] Feldman, U. 1992, Phys. Scr, 46, 202.

[64] Laming, J. 2015, Living Reviews in Sol. Phys., 12, 2.

[65] Yang, L. e. a. 2020, ApJ, 894, L6.

[66] Tian, H. e. a. 2011, ApJ, 736, 130.

[67] Dere, K. 1989, ApJ, 345, L95.

[68] Polito, V. e. a. 2015, ApJ, 803, 84.

[69] Young, P. 2015, ApJ, 801, 124.

[70] Polito, V. e. a. 2018, ApJ, 856, 178.

[71] De Pontieu, B. e. a. 2015, ApJ, 799, L12.

[72] Milligan, R. e. a. 2009, ApJ, 699, 968.

[73] Fisher, G. e. a. 1989, ApJ, 346, 1019.

[74] Reep, J. e. a. 2016, ApJ, 827, 145.

[75] Antolin, P. e. a. 2015, ApJ, 806, 81.

[76] Scullion, E. e. a. 2016, ApJ, 833, 184.

[77] Tian, H. e. a. 2011, ApJ, 736, 130.

[78] Imada, S. e. a. 2011, ApJ, 742, L18.

[79] Jeffrey, N. L. S., et al. 2021, Frontiers in Astronomy and Space Sciences, 8, 662790.

[80] Van Doorsselaere, T., et al. 2020, Space Sci. Rev., 216, 140.

[81] Testa, P., et al. 2016, ApJ, 827, 99.

[82] Cranmer, S., et al. 2008, ApJ, 677, L33.

[83] Milligan, R. O. 2011, ApJ, 740, 70.

[84] Graham, D. R., & Cauzzi, G. 2013, A&A, 551, A29.

[85] Ding, M. D., & Fang, C. 1995, ApJ, 450, L115.

[86] Rubio da Costa, F., Kleint, L., & Petrosian, V. 2016, ApJ, 827, 38.

[87] Kowalski, A. F., et al. 2017, ApJ, 836, 12.

[88] Solanki, S. K., Inhester, B., & Schüssler, M. 2006, Reports on Progress in Physics, 69, 563.

[89] Lites, B. W., et al. 2013, Sol. Phys., 283, 579.

[90] Rachmeler, L., et al. 2022, A&A, 660, A45.

[91] Rouppe van der Voort, L., et al. 2016, ApJ, 832, 52.

[92] Mariska, J. 1992, The Solar Transition Region, Cambridge University Press.

[93] Hosseini, R., Kayshap, P., Alipour, N., & Safari, H. 2024, MNRAS, 529, 3424.

[94] Mohammadiun, Z., Safari, H., & Tripathi, D. 2025, ApJ. accepted for publication.

[95] Hosseini, R., et al. 2024, Identification of the asymmetric spectral profiles in the solar transition region, J. the Earth and Space Physics.

[96] Griem, H. R. 1974, Spectral Line Broadening by Plasmas, Pure and Applied Physics, Academic Press.

[97] Rimmele, T. R., et al. 2020, Sol. Phys., 295, 1.

[98] Carlsson, M., et al. 2016, A&A, 585, A4.

[99] Delouille, V., et al. 2018, LRSP, 15, 6.

[100] Harra, L., et al. 2021, Frontiers in Astronomy and Space Sciences, 8, 662790.

[101] Patsourakos, S., et al. 2020, Space Sci. Rev., 216, 131.

[102] Judge, P., et al. 2015, ApJ, 808, 116.

[103] Young, P. R. 2011, ApJ, 744, 14.

[104] Velli, M., et al. 2020, A&A, 642, A1.

[105] Asensio Ramos, A., & Díaz Baso, C. J. 2018, A&A, 614, A5.

[106] Camporeale, E. 2019, Space Weather.